Journal of Materials Chemistry A

Thermally Robust and Strongly Oxidizing Surface of WO_3 Hydrate Nanowires for Electrical Aldehyde Sensing with Long-Term Stability

Journal:	*Journal of Materials Chemistry A*
Manuscript ID	TA-ART-11-2020-011287.R1
Article Type:	Paper
Date Submitted by the Author:	20-Dec-2020

Complete List of Authors:	Zhang, Guozhu; The University of Tokyo, Department of Applied Chemistry Hosomi, Takuro; The University of Tokyo, Department of Applied Chemistry Mizukami, Wataru; Osaka University, Institute for Open and Transdisciplinary Research Initiatives Liu, Jiangyang; The University of Tokyo, Department of Applied Chemistry Nagashima, Kazuki; The University of Tokyo, Department of Applied Chemistry Takahashi, Tsunaki; The University of Tokyo, Department of Applied Chemistry Kanai, Masaki; Kyushu University, Institute for Materials Chemistry and Engineering Sugiyama, Takeharu; Kyushu University, Research Center for Synchrotron Light Applications Yasui, Takao; Nagoya University, Department of Applied Chemistry Aoki, Yuriko; Kyushu University, Faculty of Engineering Sciences, Department of Material Sciences Baba, Yoshinobu; Nagoya University, ImPACT Research Center for Advanced Nanobiodevices Ho, Johnny; City University of Hong Kong, Department of Physics and Materials Science Yanagida, Takeshi; The University of Tokyo, Department of Applied Chemistry

ARTICLE

Received 00th January 20xx,

Accepted 00th January 20xx

DOI: 10.1039/x0xx00000x

Thermally Robust and Strongly Oxidizing Surface of WO_3 Hydrate Nanowires for Electrical Aldehyde Sensing with Long-Term Stability

Guozhu Zhang,[ab] Takuro Hosomi,[ac] Wataru Mizukami,[cde] Jiangyang Liu,[ab] Kazuki Nagashima,[ac] Tsunaki Takahashi,[ac] Masaki Kanai,[ab] Takeharu Sugiyama,[f] Takao Yasui,[cg] Yuriko Aoki,[b] Yoshinobu Baba,[g] Johnny C Ho,[bh] Takeshi Yanagida[a,b]*

Electrical molecular nanosensors require two conflicting surface characteristics, including a catalytic activity for molecular selectivity and a thermal stability for long-term data collection. Here, we show that a simple surface treatment using strong acids creates such two conflicting surface properties of WO_3 hydrate nanowires to enhance the electrical molecular sensing of aldehydes (nonanal as biomarker). Mass-spectrometric measurements reveal that the surface treatment using strong acids substantially promotes both the oxidization of nonanal and the desorption of products-nonanoic acid from the surfaces at temperature-50°C, which is lower than 300°C required for untreated surfaces. Spectroscopic and structural measurements combined with numerical simulations identify the two different adsorption structures of carbonyl groups on the surface, of which molecules directly bound to coordinatively unsaturated surface tungsten preferentially proceed to the catalytic oxidization reaction and subsequent desorption process. Furthermore, we confirm the thermal durability (over 10 years) of catalytic activity on acid-surface treated WO_3 hydrate nanowire surfaces up to 300°C, which enables us to demonstrate the long-term stable sensor operations with the sensitivity (4 orders of magnitude) over years.

Introduction

Electrical molecular sensing of various chemical species recently offers new scientific and industrial approaches to understand inherently complex systems (biological activity, chemical processing, human metabolism and others) via analyzing collected chemical big-data, which can be further combined with available existing data using physical sensors.[1-5] Among various molecular sensing methods, heterogeneous catalysis-based molecular sensing is particularly promising for such electrical molecular sensing devices for a long-term data collection.[6-8] This is because such heterogeneous catalysis on solid surfaces exhibits the molecular transformations with the electron transfers,[9] which essentially enhance the molecular sensitivity and selectivity in recorded electrical signals.[9-11] To improve heterogeneous catalysis-based electrical molecular sensing, there are inherently two requirements, which are a catalytic activity for molecular selectivity and a thermal robustness for a long-term data collection.[12-14] Because in general a catalytic activity tends to deactivate over time, especially when sensing under high temperature range.[15,16] This would greatly limit the practice applications of such kind of molecular sensors for the trace molecule (ppb to ppt level) detection and discrimination, for example, trace nonanal (aldehyde, lung cancer biomarker) detection from the exhaled breath for lung cancer early screening and diagnose.[17] Thus, satisfying both a catalytic activity and a thermal robustness on sensor surfaces is essential to design long-term stable molecular nanosensors using catalysis.

To fulfill these two requirements, previous studies as to heterogeneous catalysis-based electrical molecular sensing have utilized various nanostructures, including thermal robust metal oxides,[18,19] noble metal nanostructures supported on metal oxides[20-22] and heterostructures[23-25]. For example, nanostructured metal oxides have been tailored by intentionally introducing oxygen vacancies to enhance the catalysis for electrical molecular sensing.[26-28] Nobel metal nanostructures on metal oxide surfaces exhibit so-called spillover effects for gas molecules, which enhance the catalysis and the electrical molecular sensing.[20,29,30] Heterostructures are also promising candidates to enhance catalysis-based electrical molecular sensing via the presence of hereto-interface, where a built-in electric potential exists.[7,23-25] Although these nanostructures are practically useful for heterogeneous

[a] Department of Applied Chemistry, Graduate School of Engineering, The University of Tokyo, 7-3-1, Hongo, Bunkyo-ku, Tokyo, 113-8654, Japan
[b] Institute for Materials Chemistry and Engineering, Kyushu University, 6-1 Kasuga-Koen, Kasuga, Fukuoka, 816-8580, Japan
[c] JST-PRESTO, 4-1-8 Honcho, Kawaguchi, Saitama 332-0012, Japan
[d] Center for Quantum Information and Quantum Biology, Institute for Open and Transdisciplinary Research Initiatives, Osaka University, Osaka 560-8531, Japan
[e] Graduate School of Engineering Science, Osaka University, 1-3 Machikaneyama, Toyonaka, Osaka 560-8531, Japan.
[f] Research Center for Synchrotron Light Applications, Kyushu University, 6-1 Kasuga-koen, Kasuga, Fukuoka 816-8580, Japan
[g] Graduate School of Engineering, Nagoya University, Furo-cho, Chikusa-ku, Nagoya 464-8603, Japan
[h] Department of Materials Science and Engineering, State Key Laboratory of Terahertz and Millimeter Waves, and Centre for Functional Photonics, City University of Hong Kong, Kowloon 999077, Hong Kong SAR

†Electronic Supplementary Information (ESI) available: [details of any supplementary information available should be included here]. See DOI: 10.1039/x0xx00000x

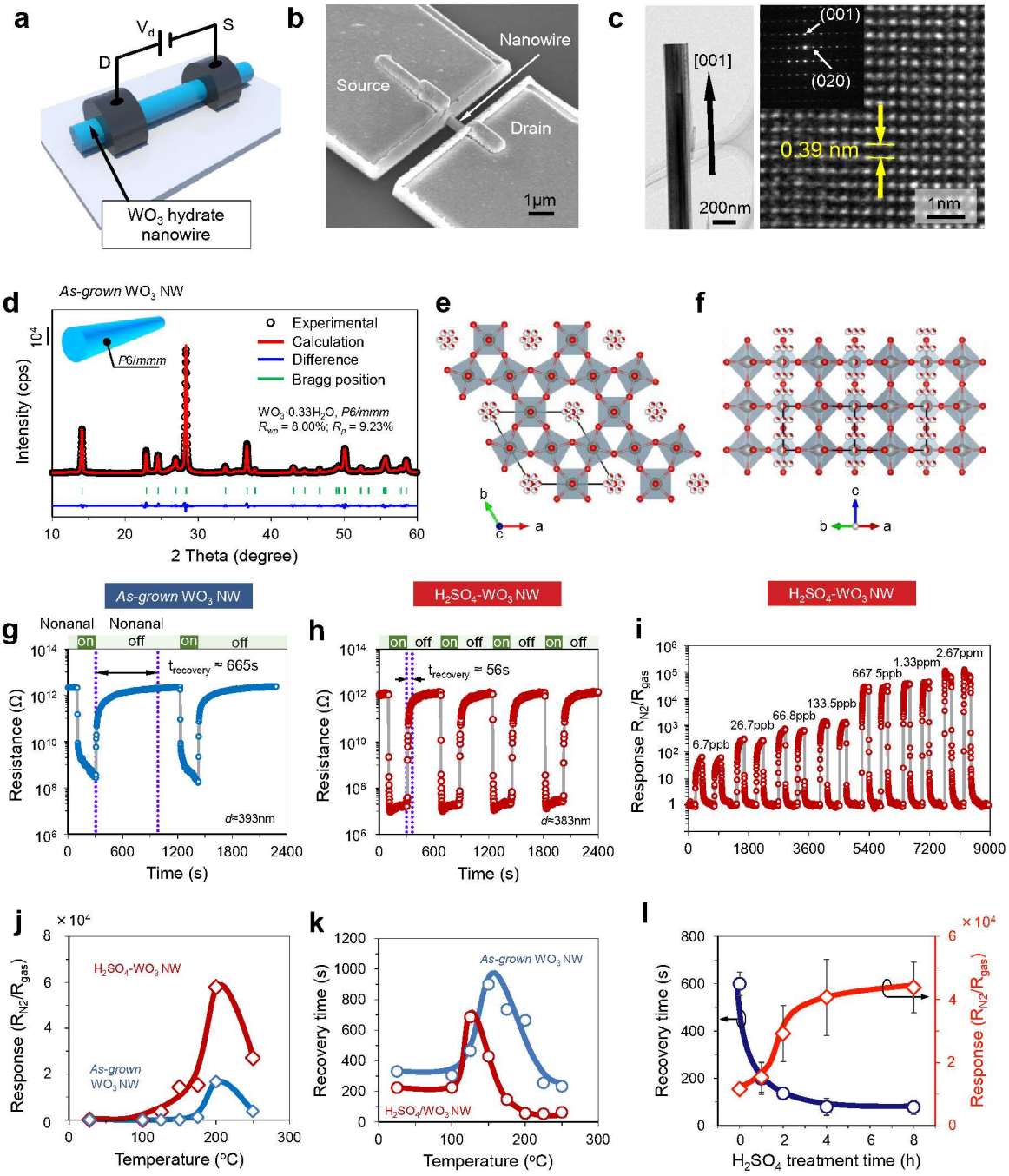

Figure 1. (a) Schematic illustrations and (b) SEM images of single WO_3 hydrate nanowire sensor device. (c) The transmission electron microscopy (TEM) and selected area electron diffraction (SAED) images of a WO_3 hydrate nanowire. (d) X-ray diffraction (XRD) pattern and the Rietveld refinement of *as-grown* WO_3 hydrate nanowires. Projections of *as-grown* WO_3 hydrate nanowires along the (e) *c* axis and (f) the [110] direction. The red sectors in water "dots" represent the probability of water's presence at the corresponding sites. (g) and (h) are sensor response data of both *as-grown* and H_2SO_4-surface treated WO_3 hydrate nanowire sensors when introducing nonanal of 2.67 ppm at 200 °C. Recovery time is defined as the time required to obtain the 90% original resistance value. (i) Dynamic resistance response of H_2SO_4-surface treated WO_3 nanowire sensor device to various concentration (from 6.7 ppb to 2.67 ppm) of nonanal at 200 °C (Figure S2). (j) and (k) are temperature-dependent sensing response and recovery time of *as-grown* and H_2SO_4-surface treated WO_3 nanowire sensor devices to 2.67 ppm nonanal (Figure S3). (l) Recovery time and sensing response of the WO_3 hydrate single nanowire device at 200 °C when varying the surface acid treatment time (Figure S5).

catalysis-based molecular sensing, designing and tailoring long-term stability catalysts for molecular sensing are still based on a rule of thumb mainly due to the lack of knowledge as to complex molecular transformation behaviors on nanostructured catalyst surfaces and the correlation between molecule behaviors, surface structures and recorded electrical signals.[21,22-30] For these reasons, various operando methodologies, including diffuse reflectance infrared Fourier transform spectroscopy (DRIFT), Raman, UV/Vis, X-ray absorption spectroscopy and X-ray diffraction, have been introduced to understand mechanisms of heterogeneous catalysis-based electrical molecular sensing.[31-35] For example, operando DRIFT method is a powerful technique for on-line analysis of molecular reaction products on the sensor surface.[31,36-39] These operando techniques frequently sacrifice their sensitivity and resolution for the in-situ operations.[31,36-39] We have recently reported a methodology to monitor surface molecular transformation behaviors, which is sensitive enough even for relatively low-density molecules adsorbed on nanostructured oxides, using a combined technique of infrared *p*-polarized multiple-angle incidence resolution spectroscopy and temperature programmed desorption/gas chromatography mass spectrometry.[40]

In this study, we demonstrate thermally robust and catalytically active sensor surfaces of WO_3 hydrate nanowires for electrical aldehyde (nonanal) sensing by monitoring their surface molecular transformation behaviors under sensing environments. Mass-spectrometric, spectroscopic and structural measurements combined with numerical simulations reveal the presence of thermally robust coordinatively unsaturated tungstens on WO_3 hydrate nanowire surfaces.

Results and discussion

First, we show the effect of surface treatment using sulfuric acid (H_2SO_4) on the electrical response data of WO_3 hydrate nanowire sensor. Figure 1a and 1b show the schematic image and scanning microscope image (SEM) of fabricated sensor device composed of a single WO_3 hydrate nanowire and Pt electrodes. The transmission electron microscopy (TEM) and selected area electron diffraction (SAED) images of fabricated WO_3 hydrate nanowires are shown in Figure 1c, revealing that the *as-grown* nanowire is a single crystalline hexagonal crystal structure and the growth direction can be assigned to be [001]. Figure 1d shows the XRD data, which reveals the WO_3 hydrate crystal structure ($WO_3{\cdot}nH_2O$), as illustrated in Figure1 e and f. In the single nanowire sensor device, the open-top gap between electrodes was designed to be 1 μm. The details of sensor device fabrication processes can be seen in Method section. We performed a surface treatment for *as-grown* WO_3 hydrate nanowires using sulfuric acid (H_2SO_4 conc.) for 4 h (Figure S1, SEM data). Figure 1g and 1h show the comparison between 1) the sensor device composed of *as-grown* WO_3 nanowire and 2) the sensor device composed of H_2SO_4-surface treated WO_3 nanowire on the electrical response data when introducing nonanal of 2.67 ppm. The operating temperature was 200 °C. As can be seen, the surface treatment significantly enhances the sensor electrical response and the recovery rate. We confirm this significant effect of surface acid treatment on both the nonanal concentration dependence data (Figure 1i) and the operating temperature dependence data (Figure 1j and 1k). The acid surface treated sensor device exhibits the detectable electrical response down to 6.7 ppb which is two times lower than that of *as-grown* WO_3 hydrate nanowire sensor (13.4, Figure S2). Note that the observed nonanal sensing performance of the acid surface treated WO_3 nanowire sensor device is superior in sensitivity and ultralow in detection limit to previously reported nonanal sensors as summarized in Supporting Information Table S1. In addition, molecular sensing selectivity evaluation has shown that the acid surface treated sensor presents a selectivity to nonanal (Figure S4). To further confirm the effect of surface acid treatment, the surface treatment time dependence on the sensor properties (sensor response ratio and recovery time data) are shown in Figure 1l. Clearly, increasing the surface acid treatment time improves the sensor properties (*i.e.* increasing the sensor response and decreasing the sensor recovery time). Thus, the simple surface

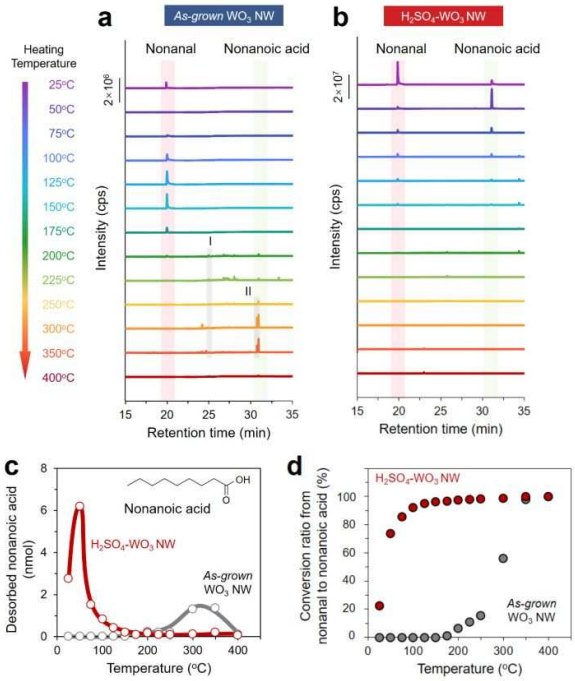

Figure 2. (a) and (b) TPD-GCMS spectra of desorbed molecules from as-grown WO_3 hydrate nanowire surfaces and H_2SO_4-surface treated WO_3 hydrate nanowire surfaces when elevating a temperature from 25 to 400 °C. The desorption products from as-grown WO_3 hydrate nanowires at retention time of 25.0 min and 30.8 min are corresponding to 8-heptadecene (I) and 9-heptadecanone (II), respectively. (c) Calculated concentration data of desorbed nonanoic acid (nmol) from as-grown WO_3 hydrate nanowire surfaces and H_2SO_4-surface treated WO_3 hydrate nanowire surfaces. The nonanoic acid calibration curve is shown in Figure S9. (d) Comparison between as-grown WO_3 hydrate nanowires and H_2SO_4-surface treated WO_3 hydrate nanowires on conversion ratio from nonanal to nonanoic acid as a function of temperature.

treatment using H_2SO_4 significantly improves the electrical response behaviors of WO_3 hydrate nanowire sensors.

Since the observed electrical response in Figure 1 is inherently determined by the surface chemical reaction events, we performed temperature-programmed desorption/gas chromatography mass spectrometry (TPD-GCMS) to analyze chemical compositions of the desorbed molecules from nonanal-adsorbed WO_3 hydrate nanowire surfaces, as shown in Figure 2a, b. The temperature-dependent chromatograms show that not only nonanal (Retention time, 19.8min. Figure S7) but also nonanoic acid (Retention time, 31.1min. Figure S7) are included in the desorbed molecules, which elucidates the progress of nonanal oxidation on the WO_3 hydrate nanowire surface. Interestingly, there are several distinct differences in these oxidation and desorption behaviors between *as-grown* WO_3 hydrate nanowires and H_2SO_4-surface treated WO_3 hydrate nanowires. First, the temperature range where a nonanoic acid is detected in the chromatograms is much lower in the case of H_2SO_4-surface treated WO_3 hydrate nanowires (mainly at 25-75°C), when compared to *as-grown* WO_3 hydrate nanowires (mainly at 250-350°C) (Figure 2c). Nonanal is almost fully converted into nonanoic acid below 50 °C on the H_2SO_4-surface treated WO_3 hydrate nanowires. It is contrast to the case of *as-grown* WO_3 hydrate nanowires, in which nonanal remains up to 175 °C (Figure 2d). These results highlight the superior oxidative activity of the surface treated WO_3 hydrate nanowires even at a low temperature range. Second, at high temperature range (200-350 °C), some olefins and ketones (Figure S8) are desorbed only from *as-grown* WO_3 hydrate nanowires. These compounds are considered to be formed by thermal decomposition of nonanoic acid,[41,42] which remain adsorbed even in such a high temperature range. These results highlight that the adsorption of the molecules is much stronger on the *as-grown* WO_3 hydrate nanowires than that of surface treated WO_3 hydrate nanowires. These trends of desorbed chemical species give an information as to surface chemical events related to the electrical sensor responses in Figure 1. *i.e.*, 1) the superior catalytic characteristics of surface treated WO_3 hydrate nanowires improves the sensing characteristics, and 2) the residual compounds on *as-grown* WO_3 hydrate nanowire surface lengthen the recovery time even at the higher temperatures.

Although above TPD-GCMS data identify the desorbed chemical compounds related to surface chemical reactions, they are not direct information of chemical events on sensor surfaces. Thus, we perform Fourier transform infrared spectroscopy (FT-IR) spectroscopy measurements on the sensor surface to reveal more directly surface molecular transformation behaviors under sensing environments. Figure 3a and b show the comparison between *as-grown* WO_3 hydrate nanowires and H_2SO_4-surface treated WO_3 hydrate nanowires on the temperature dependent FT-IR spectra in the temperature range from 25 to 400°C at atmospheric environments. Clearly, there are several distinct differences between the two spectra.

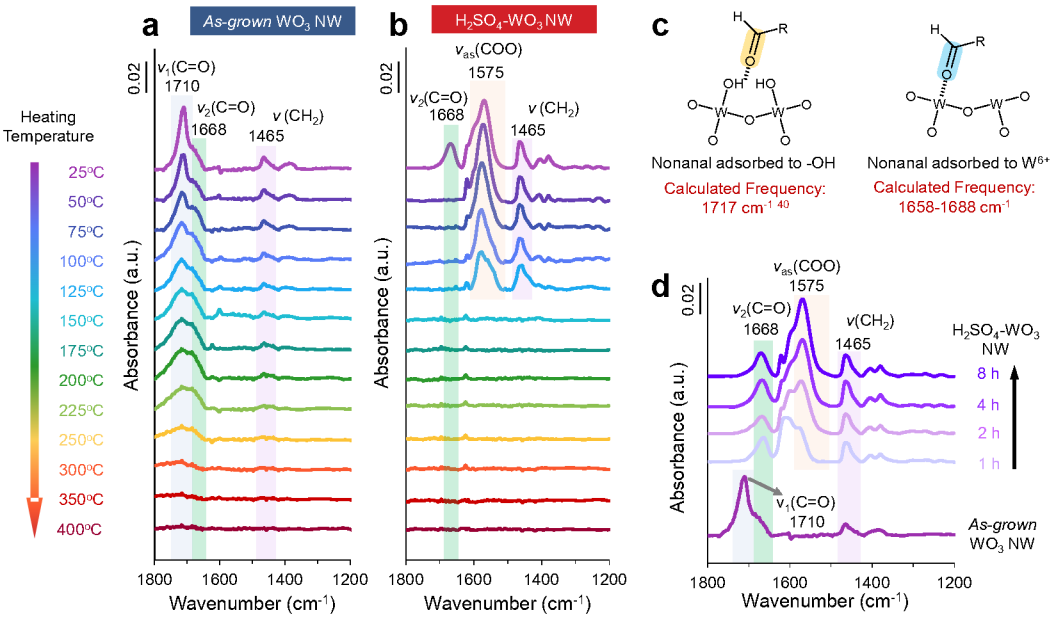

Figure 3. (a) and (b) FT-IR spectra of nonanal adsorption on *as-grown* WO_3 hydrate nanowires and H_2SO_4-surface treated WO_3 hydrate nanowires when elevating a temperature from 25-400 °C. (c) Schematic structures of surface-adsorbed nonanal and corresponding density functional theory (DFT)-calculated C=O frequencies (see the Supporting Information for details of the theoretical calculations). (d) FT-IR spectra of nonanal adsorption on WO_3 hydrate nanowires with different treatment time by H_2SO_4.

First, the difference on two peaks (ν_1 and ν_2) in the 1660-1740 cm^{-1} region reveals two distinct adsorption states of carbonyl group, which depends on the surface acid treatment. The two peaks (ν_1-1710 cm^{-1} and ν_2-1668 cm^{-1}) can be associated to the

ν (C=O) vibration mode.[43] Compared to the FT-IR spectrum of liquid-phase nonanal- (ν (C=O)-1726 cm^{-1}),[40] both ν_1(C=O) and ν_2 (C=O) show clear red shifts, implying decreases of C-O bond orders via Lewis acidic activation.[40,44] Our previous work also revealed that nonanal adsorbed on the surface –OH of a metal oxide (ZnO) shows the adsorption at 1709 cm^{-1}.[40] Thus, we assigned ν_1(C=O) to nonanal adsorbed via hydrogen bonding with a surface -OH. On the other hand, the much larger redshift of ν_2 (C=O) implies that C=O is activated by stronger Lewis acids. Therefore, we assigned ν_2 (C=O) to nonanal adsorbed by coordination to a surface exposed W^{6+}(Figure 3c). A theoretical calculation based on the density functional theory (DFT) also supports this assignment (Figure S10). The wavenumber of a simplified structure of W^{6+}-coordinated nonanal is calculated to be 1658-1688 cm^{-1}, which is in good agreement with the experimental value (1668 cm^{-1}). Based on these peak assignments, we discuss the effect of surface acid treatment on the ν_1 (C=O) and ν_2 (C=O) peaks. As can be seen in Figure 3, at 25°C, *as-grown* WO_3 hydrate nanowires showed only ν_1(C=O) peak, whereas H_2SO_4-surface treated WO_3 hydrate nanowires exhibited only ν_2 (C=O) peak. This distinct difference can be reasonably interpreted in terms of above assignments of ν_1 (C=O) and ν_2 (C=O) peaks on the surface molecular structures. On H_2SO_4-treated WO_3 hydrate nanowire surfaces, the stronger Lewis acid site (bare surface W) exists to show ν_2 (C=O) peak, whereas for *as-grown* WO_3 hydrate nanowires, -OH terminated surface promotes to exhibit ν_1(C=O) peak. Thus, these results highlight that the two distinct adsorption states of carbonyl group exist, which strongly depend on the history of surface acid treatment on WO_3 hydrate nanowires.

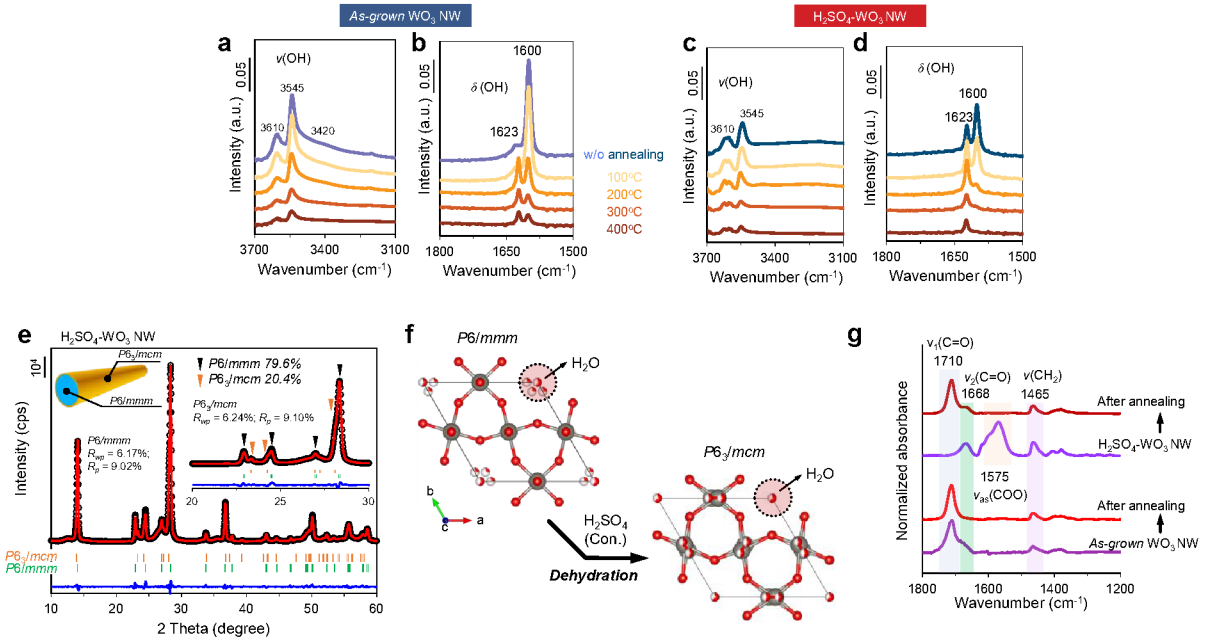

Figure 4. (a)-(d) FT-IR spectra of as-grown WO_3 nanowires and H_2SO_4-surface treated WO_3 nanowires after thermally treated with different temperature. (e) X-ray diffraction (XRD) pattern and the Rietveld refinement of H_2SO_4-surface treated WO_3 nanowires. (f) Refined crystal structure unit of as-grown WO_3 hydrates and H_2SO_4-surface treated WO_3 hydrates, where the red sectors in water "dots" represent the probability of water's presence at the corresponding sites (other viewports are shown in Figure S13). (g) FT-IR spectra of nonanal adsorbed on the 400 °C annealed as-grown WO_3 nanowires H_2SO_4-surface treated WO_3 nanowires.

Second, the broad peak in the 1550-1600 cm^{-1} region in Figure 3, which appeared only for surface treated WO_3 hydrate nanowires, reveals the presence of carboxylate compounds on WO_3 hydrate nanowire surface.[38,45] Previous studies have identified that the broad peak in the 1550-1600 cm^{-1} region corresponds to an asymmetric stretching vibration mode: ν_{as} (COO) of carboxylate compounds, which strongly bound to solid surfaces.[46,47] This peak was not observable for *as-grown* WO_3 hydrate nanowires at all. In other words, such carboxylate compounds only exist on H_2SO_4 treated WO_3 hydrate nanowire surface. To further confirm the effect of H_2SO_4 treatment on the appearance of surface carboxylate compounds, we measured the dependence of H_2SO_4 treatment time on FT-IR spectra, as shown in Figure 3d. As can be seen, the peak intensity in the 1550-1600 cm^{-1} region tended to increase with the H_2SO_4 treatment time, revealing the significant effect of surface treatment on the appearance of surface carboxylate compounds. This also can be demonstrated by the time-dependent FT-IR measurement (Figure S11). In addition, as seen in Figure 3b, the surface carboxylate compounds desorbed at relatively low temperatures below 125 °C, which is consistent with the desorption profile of nonanoic acid for surface treated WO_3 hydrate nanowires in Figure 2c. On the other hand, in Figure 3b, ν_1 (C=O) peak for *as-grown* WO_3 hydrate nanowires remains even at higher temperatures up to 350 °C. These temperature dependences of carbonyl groups and carboxylate

compounds on the spectroscopic data are in good agreement with TPD-GCMS data in Figure 2, revealing the detailed molecular transformation behaviors on WO_3 hydrate nanowire surface during the desorption process.

Above mass-spectrometric and spectroscopic results explain the effect of surface acid treatment on the molecular sensing properties (Figure 1) in terms of the surface molecular transformation behaviors on WO_3 hydrate nanowire surface. However, we still cannot answer the following simple question, what are surface structures created by H_2SO_4 treatment, which improve the catalytic characteristics. To identify the mechanisms of catalytic surface structures, first we focus on the surface conditions before nonanal adsorption. It is noted that the spectroscopic data in Figure 3 do not contain any experimental trends as to water molecules on the sensor surface. This is because their spectra are intentionally subtracted by a spectrum of sample before nonanal adsorption to exclude background moisture effects on the spectra. Figure 4a-d show raw FT-IR spectra of *as-grown* WO_3 hydrate nanowires and H_2SO_4-surface treated WO_3 hydrate nanowires before nonanal adsorption. The annealing temperature effects on the spectra are also shown in the Figure4 a-d, since sensing experiments were performed at elevated temperatures up to 300°C. As can be seen, there are distinct peaks of water molecules, which are ranged at 3500-3700 cm^{-1}: a stretching mode of OH-ν_{OH}, and 1595-1650 cm^{-1}: a bending mode of OH-δ_{OH}.[43] Clearly, increasing the annealing temperature decreases the amount of water, and the H_2SO_4 treatment further enhances the removal of a water from solid samples due to a strong hydration effect to SO_4^{2-}.[48,49] Thus, there is a difference of water content between *as-grown* WO_3 hydrate nanowires and H_2SO_4-surface treated WO_3 hydrate nanowires. In addition, at elevated temperatures of sensing conditions, water related peaks almost disappeared for H_2SO_4-surface treated WO_3 hydrate nanowires, but not for *as-grown* WO_3 hydrate nanowires. In the 1595-1650 cm^{-1} region, there are two distinct peaks of δ_{OH}. The peak at 1595-1600 cm^{-1} is associated to δ_{OH} of $WO_3 \cdot 2H_2O$, and the peak at 1620-1625 cm^{-1} can be assigned to δ_{OH} of $WO_3 \cdot H_2O$.[50] XRD measurements for these samples also show the presence of tungsten trioxide hydrates ($WO_3 \cdot xH_2O$) (Figure S12-S14) and the dehydration behaviors when annealing (Figure S15) and acid treatment were performed, as shown in Figure 4e. Thus, results in Figure 4a-e consistently indicate that H_2SO_4 surface treatment dehydrates WO_3 hydrate nanowires more than *as-grown* WO_3 hydrate nanowires at elevated temperature range of sensing conditions. This difference of water content in WO_3 hydrate nanowires might affect the absorption and desorption behaviors. Therefore, the first possible model is based on the presence of water molecules near surfaces. This is because the presence of water near surfaces might hinder an interaction between a carbonyl group and a Lewis acid site of surface W. As seen in the spectra of Figure 4a-d, the thermal annealing alters the water content of WO_3 hydrate nanowires. Therefore, we can examine the effect of water content on the molecular transformation behaviors by using such annealed WO_3 hydrate nanowires. If the water content of WO_3 hydrate nanowires solely dominates surface molecular transformation behaviors of nonanal, the annealed WO_3 hydrate nanowires, which are dehydrated, should exhibit the catalytic and molecular behaviors similar to H_2SO_4-surface treated samples. Figure 4g shows the spectra of the nonanal adsorption on the annealed WO_3 hydrate nanowires. Contrary to above our speculation, the spectra are similar to that of *as-grown* WO_3 hydrate nanowires. As shown in Supplemental data (Figure S16), the electrical sensing response of annealed WO_3 hydrate nanowires is also similar to that of *as-grown* WO_3 hydrate nanowires on the recovery time although the electrical responses are enhanced. Thus, the difference of water content in WO_3 hydrate nanowires alone cannot explain the occurrence of enhanced catalytic characteristics by surface acid treatment.

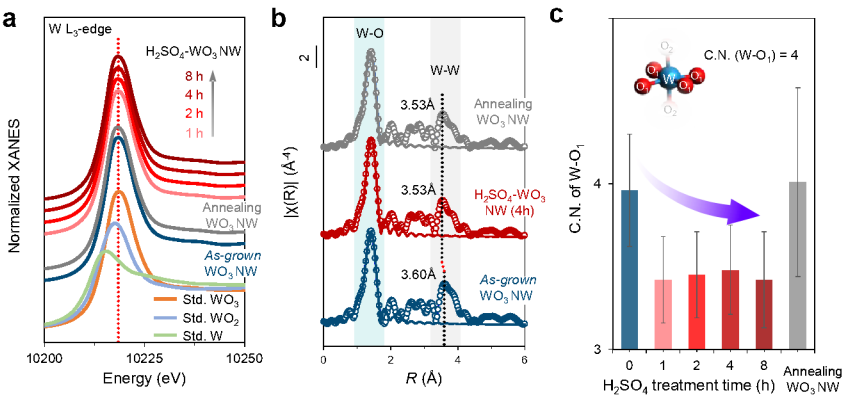

Figure 5. (a) Normalized W L_3-edge XANES spectra of WO_3 hydrate nanowires and the standard W, WO_2 and WO_3 (Sigma Aldrich) as reference. (b) Fourier transformed k^3-weighted $\chi(k)$-function of the EXAFS spectra (circles) and first-shell fittings (line) of WO_3 hydrate nanowires. The detailed fitting processes are shown in the Supporting Information. (c) W coordination numbers (C.N.) of first shell extracted from Fourier transformed EXAFS curve fitting.

Here, we focus on the observed difference between a surface acid treatment and a thermal annealing on a dehydration process of WO_3 hydrate nanowires to clarify the mechanisms of surface acid treatment. Thermal annealing physically removes a

water from a solid at elevated temperatures, whereas surface acid treatment chemically dehydrates WO_3 hydrate nanowires at relatively low temperatures by utilizing the strong hydration effect to SO_4^{2-}.[48,49] It is easily inferred that a high temperature operation of thermal annealing process creates a thermodynamically stable solid surface structure, while a low temperature operation of chemical surface acid treatment might exhibit thermodynamically unstable solid surface structures.[51,52] Extended X-ray absorption fine structure (EXAFS) analysis for a coordination structure of W can reveal such surface solid structure difference.[53-55] Figure 5a shows normalized W L_3-edge X-ray absorption near edge structure (XANES) of the WO_3 hydrate nanowire samples after H_2SO_4 surface treatment and thermal annealing treatment (400 °C). It can be seen that the peaks of all WO_3 hydrate nanowires are consistent with the standard WO_3 (10218.5 eV), indicating the oxidization states of W of the treated WO_3 hydrate nanowire samples do not change. This is also supported by the XPS characterizations (Supporting Information, Figure S17). Furthermore, the Fourier transform (FT) $k^3\chi(k)$ spectra of the WO_3 nanowire samples exhibit a dominant peak centered at 1.40 Å assignable to the W-O bond, and W-W bond peak centered at 3.60 Å (Figure 5b). In addition, the FT spectra of surface treated WO_3 hydrate nanowires showed that the W-W peaks undergo a downshift to 3.53 Å as compared to that of *as-grown* WO_3 hydrate nanowires, indicating that lattice contraction occurred due to the dehydration effect. Figure 5c shows the averaged coordination number data of the first shell of W ion from the fitting of FT $k^3\chi(k)$ spectra. The analyzed coordination number of W tends to decrease as the H_2SO_4 surface treatment time increases, while the annealing treatment has negligible effects on the coordination number of W. These results reveal the presence of coordinatively unsaturated W for H_2SO_4 surface treated WO_3 hydrate nanowires, but not for thermally annealed WO_3 hydrate nanowires. Thus, above all spectroscopic results highlight that the presence of coordinatively unsaturated W of WO_3 hydrate nanowires plays an essential role on promoting the catalytic effects and molecular sensing properties in Figure 1.

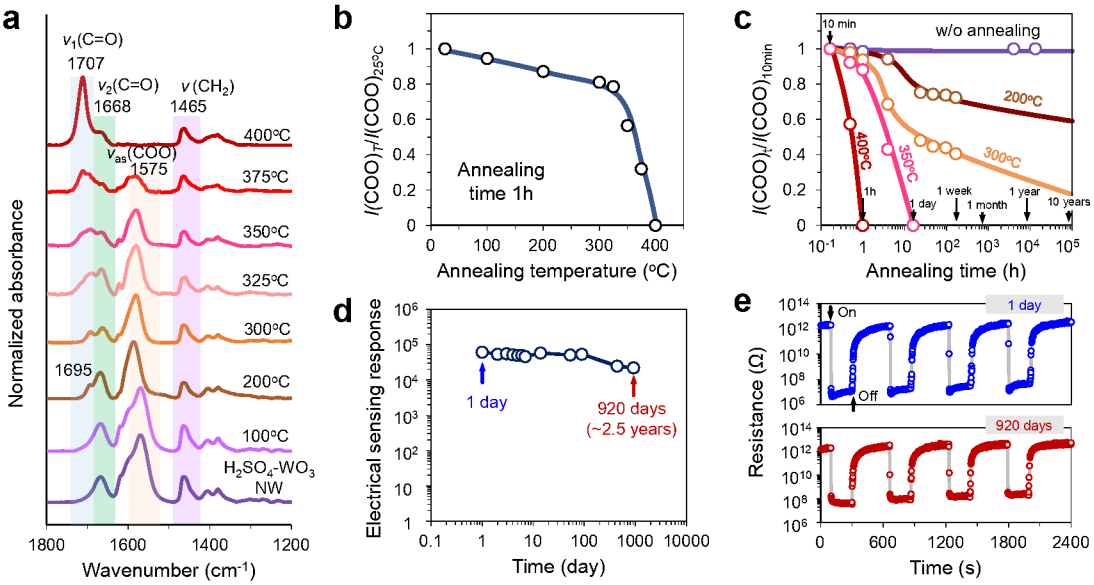

Figure 6. (a) Temperature dependence of FT-IR spectra of H_2SO_4 surface treated WO_3 hydrate nanowire catalysis. The annealing time is 1 hour. (b) Temperature dependence of the ratio between the intensity of ν_{as}(COO) after annealing ($I(COO)_T$) and without annealing ($I(COO)_{25°C}$), which are extracted from (a) data. (c) Time series data of catalysis degradation when varying the temperature ($I(COO)_t$, intensity of ν_{as}(COO) after annealing for designed time; $I(COO)_{10min}$, intensity of ν_{as}(COO) after annealing for 10 minutes). The raw data of FT-IR are shown in Supporting Information (Figure S19-S20). (d) Long-term stability of H_2SO_4 surface treated WO_3 hydrate nanowire sensor device (working at 200 °C, nonanal, 2.67 ppm. Supporting Information Figure S21). (e) Dynamic resistance response of H_2SO_4 surface treated WO_3 hydrate nanowire sensor device after stored in air for 1 day and 920 days.

Finally, we examine the thermal durability of surface-treated WO_3 hydrate nanowire catalysts. Figure 6a shows the thermal durability (air-annealing temperature dependence) data on IR spectra of H_2SO_4 surface treated WO_3 hydrate nanowires under sensing environments-atmospheric air and temperature range. The air-annealing time is 1 hour. Figure 6b shows the extracted thermal durability data of ν_{as} (COO) peak as an index of catalytic properties (an oxidization of nonanal) of WO_3 hydrate nanowires. The data are shown as the ratio of ν_{as} (COO) peak at annealed temperature to that at 25°C. As can be seen, the catalytic properties by acid surface treatments can be maintained up to 300°C of annealing temperature, which is robust enough required for electrical sensing. To further examine the robustness as a time series, Figure 6c shows the

time series data of ratio of ν_{as} (COO) peaks during durability tests for various annealing temperatures. The data are shown as the ratio of ν_{as} (COO) peak at annealing time to that at 10 minus- annealing time. For the temperature range for molecular sensing experiments around 200 °C (Figure 1), the catalytic effect can be maintained at least over 10 years. Even at higher temperature range up to 300°C, the catalytic activity remains over a year. Considering the surface catalytic mechanisms discussed in previous sections, this observed thermal robustness of tailored catalytic surfaces corresponds to the thermal stability of coordinatively unsaturated W of WO_3 hydrate nanowires. In addition, we examine the long-term stability of H_2SO_4 surface treated WO_3 hydrate nanowire sensors for nonanal, as shown in Figure 6d and 6e. As can be seen, the electrical sensing response can be maintained over 2.5 years with keeping the electrical sensitivity (4 orders of magnitude change). This long-term stable sensing data are well consistent with the catalytic activity data in Figure 6c. Thus, these time series data quantitatively show the thermal robustness of the surface-treated WO_3 hydrate nanowire catalysis over years under sensing environments.

Conclusions

In summary, we show that a simple surface treatment using strong acids enhances both the thermally robust catalysis and electrical molecular sensing of WO_3 hydrate nanowires for carbonyl compounds. Mass-spectrometric measurements reveal that the surface treatment using strong acids substantially promotes both the oxidization of nonanal and the desorption of products-nonanoic acid from the surfaces. Spectroscopic and structural measurements combined with numerical simulations identify the two different adsorption structures of carbonyl groups on the surface, of which molecules directly bound to coordinatively unsaturated surface tungsten preferentially proceed to the catalytic oxidization reaction and subsequent desorption process. Furthermore, we confirm the thermal durability (over 10 years) of catalytic activity on acid-surface treated WO_3 hydrate nanowire surfaces up to 300°C, which enables us to demonstrate the long-term stable sensor operations with the sensitivity (4 orders of magnitude) over years. Thus, the present approach will support a better understanding and tailoring of complex nanostructured metal oxide surfaces for further sophisticated thermally robust electrical molecular sensing using heterogeneous catalysis.

Experimental

Fabrication of WO_3 hydrate nanowire. WO_3 hydrate nanowires were fabricated by two steps, which include the polytungstic acid sol synthesis and the nanowire growth.[56] For polytungstic acid (H_2WO_4) sol synthesis, tungsten powder (4g) (SIGMA-ALDRICH, 99.9%) was dissolved into hydrogen peroxide solution (H_2O_2, 30 wt. % in H_2O) (FUJIFILM Wako Pure Chemical Corp., 30.0%~35.5%) with an ice bath under continuous stirring. When W powders were dissolved, a Pt foil was added into the solution to catalytically remove the unreacted H_2O_2. As no bubble generated, the concentration of as-synthesized W precursor solution was controlled by the deionized (DI) water. Afterward, 50 mL of W precursor (10.88 mM) was transferred to a 100 mL capacity of Teflon beaker. Then, 0.5625 g (6.25 mM) of oxalic acid ($H_2C_2O_4$) (SIGMA-ALDRICH, 99.0%) was added to the mixture and the pH was carefully controlled to 1.68 by carefully adding sodium hydroxide (NaOH, 1 M) solution. Finally, the Teflon beaker was mounted in the autoclave system and then transferred to the furnace and kept at 200 °C for 24 h. Finally, WO_3 nanowires were obtained after ultracentrifugation and rinsed by DI water.

Acid and annealing treatment of WO_3 hydrate nanowire. Concentrated sulfuric acid (H_2SO_4) was utilized to dehydrate the *as-grown* WO_3 nanowire. The *as-grown* WO_3 hydrate nanowires were mixed with 50 mL H_2SO_4 and stirred at 90°C with different time (1, 2, 4, and 8 h). Then, the samples were carefully rinsed by DI water to remove residual H_2SO_4. Annealing treatment was conducted at 400 °C in air for 1 h.

Structure Characterization. Scanning electron microscopy (SEM) images were obtained using a JEOL JSM-7610F microscope. Transmission electron microscopy (TEM) images were acquired using a JEOL, JEM-ARM300F. X-ray diffraction (XRD) patterns were recorded with a Rigaku SmartLab diffractometer (Cu Kα, λ = 1.5406 Å, 45 kV, and 200 mA). Fourier transform infrared spectroscopy (FT-IR) spectra were measured using a Nicolet iS50 FT-IR spectrometer (Thermo Fisher Scientific) equipped with an MCT detector.

Desorbed gas analysis using Gas chromatography-mass Spectroscopy (GC-MS). A Shimadzu GCMS-QP 2010 Ultra instrument (equipped with a high polar InertCap FFAP capillary column and an OPTIC-4 inlet temperature control system) was used to analyze the desorbed compounds at each temperature. Firstly, *as-grown* and acid treatment WO_3 nanowires (The amount of nanowires were controlled at ~2 mg) were loaded on a silicon substrate with 0.2 cm × 2.0 cm and dried at 100 °C. Nonanal liquid (4 µL) was dropped in a 25 mL closed bottle and kept for 30 min to vaporize the nonanal gas. Then, the nanowire sample was transferred into a bottle filled with nonanal gas for a fixed time (10 min.) and immediately transferred into the inlet port of the GC-MS instrument for further measurements. The inlet temperature was rapidly heated (60 °C/s) to a given temperature (25-400 °C with step of 25 °C) and maintained for 10 min, then immediately cooled to 25 °C. The desorbed gas at each temperature was analyzed by mass spectroscopy. The measurements for each temperature were conducted sequentially without removing the sample from the inlet port. The detailed temperature program is shown in Figure S6.

FT-IR monitoring of molecular adsorption progress. Firstly, *as-grown* and acid treatment WO_3 nanowires (The amount of nanowires were controlled at ~50 mg) were loaded on a silicon substrate with 2 cm × 2.0 cm and dried at 100°C. Nonanal liquid (20 µL) was dropped in a 100 mL closed bottle and kept for 30 min to vaporize the nonanal gas. Then, the sample was transferred into a bottle filled with nonanal gas for a fixed time (10 min.) and immediately transferred into the FT-IR chamber for further measurements. The nonanal-adsorbed WO_3 nanowires were heated at a given temperature (25-400 °C with step of 25 °C) for 10 min and cooled to room temperature. The FT-IR spectra of the nanowires were then recorded

at room temperature on a Thermo Fisher Scientific Nicolet iS50 FT-IR spectrometer equipped with a MCT detector.

X-ray absorption spectroscopy. XANES and EXAFS analyses of W L_3-edge were performed in transmission mode at the BL 06 (Kyushu University beamline) of the SAGA-LS (Saga, Japan) with a storage ring operating at the energy of 1.4 GeV. A monochromator with two Si (111) crystals was used to scan the energy of the X-ray beam. The photon flux was 2×10^{10} photons/second. The intensities of the fluorescence X-rays were monitored by a silicon drift detector. Powder samples of the standard W, WO_2, and WO_3, and WO_3 nanowire samples were diluted with boron nitride to provide the optimum concentration and then pressed into a tablet with a diameter of 1 cm. The spectra of the prepared pellet samples were measured in the transmission mode. XANES data processing and *r*-space fitting of XAFS data were carried out by Athena and Artemis included in the Ifeffit package. Detailed fitting processes are shown in Supporting Information.

Computational analyses of molecular vibrational infrared spectra. The DFT calculations were carried out to compute the vibrational frequencies of nonanal molecules bonding on hexagonal WO_3 (100) plane. We used a simplified cluster model to mimic WO_3 (100) plane. The cluster model for the W^{6+} site model consisted of a single tungsten atom and five oxygen atoms. We fixed the atomic configurations of these two cluster models during the geometry optimizations. We employed B3LYP-D3 as the functional. According to a comparison with the results from other functional (ωB97XD, APFD, B3LYP, or B3LYP-D3), dependencies on used functional is found to be negligible in this calculation. More detailed discussion is described in the supporting information.

Fabrication of single nanowire device and molecular sensing measurement. Nanowire suspension was prepared by mixing the fabricated nanowire samples with 2-propanol with light sonication. Then, the dispersed nanowires were transferred on a 100 nm thickness of SiO_2 coated Si (100) substrate with pre-patterned contact Pt electrodes. Electron beam (EB) lithography (Elionix, ELS-S50YND) was performed at accelerating voltage of 50 kV to make the electrode patterns for bridging a single nanowire with contact electrodes using ZEP520A-7 (ZEON) as a resist. A 800 nm layer of Pt was then deposited by RF sputtering (SEINAN) in an Ar 0.4 Pa atmosphere. Afterward, lift-off (*N*, *N*-dimethylformamide) and acetone cleaning processes were conducted to complete the device fabrication. The gap size of bridged nanowire was designed to be 1 μm and the nanowires with ca. 300-400 nm diameter were chosen for all fabricated device to eliminate the variation of electrical properties caused by the device geometry. The sensing performance to nonanal was carried out by a self-made chamber combined with the Keithley 4200A-SCS Parameter Analyzer (TEKTRONIX, INC.). Resistance of the WO_3 nanowire device under N_2 was recorded as baseline (R_{N2}). The resistance upon exposure of nonanal gas (produced by bubbling liquid nonanal solution) was noted as R_{gas}, and sensing response was defined as R_{N2}/R_{gas}. The recovery time was defined as the time required for the recovery of the resistance to 90% of R_{N2} for the desorption process. All the sensing tests were carried out under a DC bias voltage of 1V. Nonanal gas was produced by bubbling liquid nonanal solution with high pure N_2, and its concentration was calibrated by the GCMS (Shimadzu GCMS-QP2010 Ultra) with temperature control system (GL Sciences, OPTIC-4). The flow rate of dry air and the nonanal gas were controlled at 200 sccm during the sensing performance tests and the testing temperature was set to vary from 25 to 250 °C. The bubbling nonanal gas was diluted 400 times to ppb level for the sensing test. 10-15 devices were fabricated for each sample to obtain statistical data.

Conflicts of interest

There are no conflicts to declare.

Acknowledgements

This work was supported by KAKENHI （18H0524） and JST-CREST (JPMJCR19I2). XANES and EXAFS analyses of W L_3-edge were performed in transmission mode at the BL 06 (Kyushu University beamline) of the SAGA-LS, Saga. The computation in this work was performed using the facilities of RIIT, Kyushu University. General Research Fund of the Research Grants Council of Hong Kong SAR, China (CityU 11211317).

Notes and references

1. Lewis, A., Edwards, P. *Nature*, 2016, **535**, 29–31.
2. Kalantar-Zadeh, K., Berean, K. J., Ha, N., Chrimes, A. F., Xu, K., Grando, D., Ou, J. Z., Pillai, N., Campbell, J. L., Brkljaca, R., Taylor, K. M., Burgell, R. E., Yao, C. K., Ward, S. A., McSweeney, C. S., Muir, J. G., Gibson, P. R. *Nat. Electron.*, 2018, **1**, 79–87.
3. Iitani, K., Chien, P., Suzuki, T., Toma, K., Arakawa, T., Iwasaki, Y., Mitsubayashi, K. *ACS Sens.*, 2018, **3**, 425−431.
4. Galstyan, V., Poli, N., D'Arco, A., Macis, S., Lupi, S., Comini, E., *J. Mater. Chem. A*, 2020, **8**, 20373-20385.
5. Wang, X. X., Li, H. Y., Guo, X., *J. Mater. Chem. A, 2020, **8**, 14482-14490.*
6. Dey, A. *Mater. Sci. Eng., B,* 2018, **229**, 206–217.
7. Miller, D. R., Akbar, S. A., Morris, P. A. *Sensor Actuat. B: Chem.,* 2014, **204**, 250−272.
8. Fu, Q., Bao, X. *Chem. Soc. Rev.,* 2017, **46**, 1842−1874.
9. Barsan, N., Weimar, U. *J. Electroceram.,* 2001, **7**, 143−167.
10. Cabot, A., Dieguez, A., Romano-Rodrıguez, A., Morante, J., Barsan, N. *Sensor Actuat. B: Chem.,* 2001, **79**, 98−106.
11. Korotcenkov, G. *Mater. Sci. Eng. B Solid-State Mater. Adv. Technol.,* 2007, **139**, 1−23.
12. Volanti, D. P., Felix, A. A., Orlandi, M. O., Whitfield, G., Yang, D.-J., Longo, E., Tuller, H. L., Varela, J. A. *Adv. Funct. Mater.,* 2013, **23**, 1759−1766.
13. Long, H., Harley-Trochimczyk, A., Pham, T., Tang, Z., Shi, T., Zettl, A., Carraro, C., Worsley, M. A., Maboudian, R. *Adv. Funct. Mater.,* 2016, **26**, 5158−5165.
14. Wang, X., Wang, Z., Zhang, J., Wang, X., Zhang, Z., Wang, J., Zhu, Z., Li, Z., Liu, Y., Hu, X., Qiu, J., Hu, G., Chen, B., Wang, N., He, Q., Chen, J., Yan, J., Zhang, W., Hasan, T., Li, S., Li, H., Zhang, H., Wang Q., Huang, X., Huang, W. *Nat. Commun.,* 2018, **9**, 3611.
15. Crabtree, R. H. *Chem. Rev.*, 2015, **115**, 127-150.

16. Goodman, E, D., Johnston-Peck, A. C., Dietze, E. M., Wrasman, C. J., Hoffman, A. S., Abild-Pedersen, F., Bare, S. R., Plessow, P. N., Cargnello. M. *Nat. Catal*., 2019, **2**, 748-755.
17. Fuchs, P., Loeseken, C., Schubert, J. K. Miekisch, W. *Int. J. Cancer*, 2010, **126**, 2663-2670.
18. Romain, A. C., Nicolas, J. *Sensor Actuat. B: Chem.,* 2010, **146**, 502-506.
19. Yang, H., Bai, X., Hao, P., Tian, J., Bo, Y., Wang, X., Liu, H. *Sensor Actuat. B: Chem.,* 2019, **280**, 34-40.
20. Zhou, Q., Xu, L., Umar, A., Chen, W., Kumar, R. *Sensor Actuat. B: Chem.,* 2019, **256**, 656-664.
21. Wang, Y., Cheng, P., Li, X., Wang, C., Feng, C., Lu, G. *J. Mater. Chem. C,* 2020, **8**, 78-88.
22. Lee, J. E., Lee, H. K., Park, H. J., Ma, A., Choi, S. Y., Lee, D. S. *Sensor Actuat. B: Chem.,* 2019*,* **292**, 289-296.
23. Zhou, Q., Zeng, W., Chen, W., Xu, L., Kumar, R., Umar, A., *Sensor Actuat. B: Chem.,* 2019, **298**, 126870.
24. Chen, Y. Z., Lee, S. H., Su, T. Y., Wu, S. C., Chen, P. J., Chueh, Y. L., *J. Mater. Chem. A*, 2019, **7**, 22314-22322.
25. Su, C., Zhang, L., Han, Y., Ren, C., Zeng, M., Zhou, Z., Su, Y., Hu, N., Wei, H., Yang, Z. *Sensor Actuat. B: Chem.,* 2020, **304**, 127347.
26. Zhu, Z., Zheng, L., Zheng, S., Chen, J., Liang, M., Tian, Y., Yang, D., *J. Mater. Chem. A,* 2018, **6**, 21419-21427.
27. Liu, S., Gao, S., Wang, Z., Fei, T., Zhang, T. *Sensor Actuat. B: Chem.,* 2019, **290**, 493−502
28. Al-Hashem, M., Akbar, S., Morris, P. *Sensor Actuat. B: Chem.,* 2019, **301**, 126845.
29. Kohl, D. *Sensor Actuat. B: Chem.,* 1990, **1**, 158−165.
30. Korotcenkov, G. *Sensor Actuat. B: Chem.,* 2005, **107**, 209−232.
31. Degler, D., Wicker, S., Weimar, U., Barsan, N. *J. Phys. Chem. C,* 2015, **119**, 11792−11799.
32. Sanze, S., Gurlo, A., Hess, C. *Angew. Chem., Int. Ed.,* 2013, **52**, 3607−3610.
33. Elger, A.-K., Hess, C. *Angew. Chem., Int. Ed.,* 2019, **58**, 15057−15061.
34. Koziej, D., Hübner, M., Barsan, N., Weimar, U., Sikora, M., Grunwaldt, J.-D. *Phys. Chem. Chem. Phys.,* 2009, **11**, 8620−8625.
35. Müller, S., Zimina, A., Steininger, R., Flessau, S., Osswald, J., Grunwaldt, J. D. *ACS Sens.,* 2020*,* **5**, 2486–2496.
36. Degler, D., Rank, S., Müller, S., Pereira de Carvalho, H. W., Grunwaldt, J., Weimar, U., Barsan, N. *ACS Sens*., 2016, **1**, 1322−1329
37. Wicker, S., Guiltat, M., Weimar, U., Hemeryck, A., Barsan, N. *J. Phys. Chem. C,* 2017, **121**, 25064−25073.
38. Staerz, A., Somacescu, S., Epifani, M., Kida, T., Weimar, U., Barsan, N. *ACS Sens.,* 2020, **5**, 1624−1633.
39. Suzuki, T, Sackmann, A., Oprea, A., Weimar, U., Barsan, N. *ACS Sens.,* 2020, **5**, 2555–2562.
40. Wang, C., Hosomi, T., Nagashima, K., Takahashi, T., Zhang, G., Kanai, M., Zeng, H., Mizukami, W., Shioya, N., Shimoaka, T., Tamaoka, T., Yoshida, H., Takeda, S., Yasui, T., Baba, Y., Aoki, Y., Terao, J., Hasegawa, T., Yanagida, T. *Nano Lett.,* 2019, **19**, 2443−2449.
41. Grant, J. L., Hsieh, C. H., Makris, T. M. *J. Am. Chem. Soc.,* 2015, **137**, 4940−3.
42. Renz, M. *Eur. J. Org. Chem.,* 2005, **2005**, 979−988.
43. George, S. *Infrared and Raman characteristic group frequencies: tables and charts* (John Wiley & Sons, 2004).
44. Zaki, M. I., Hasan, M. A., Pasupulety, L. *Langmuir,* 2001, **17**, 768−774.
45. Patrono, P., La Ginestra, A., Ramis, G., Busca, G. *Appl. Catal. A,* 1994, **107**, 249–266.
46. Papageorgiou, S. K., Kouvelos, E. P., Favvas, E. P., Sapalidis, A. A., Romanos, G. E., Katsaros, F. K. *Carbohydrate Res.,* 2010, **345**, 469−473.
47. Jia, X., Ma, J., Xia, F., Xu, Y., Gao, J., Xu, J. *Nat. Commun.,* 2018, **9** (1), 1−7.
48. JO'M, B., Gamboa-Aldeco, M., Szklarczyk, M. *J. Electroanal. Chem.,* 1992, **339**, 355−400.
49. Wang, X.B., Sergeeva, A. P., Yang, J., Xing, X.-P., Boldyrev, A. I., Wang, L. S. *J. Phys. Chem. A,* 2009, **113**, 5567−5576.
50. Daniel, M. F., Desbat, B., Lassegues, J. C., Gerand, B., Figlarz, M. *J. Solid State Chem.,* **1**987, **67**, 235− 247.
51. Krü ger, P., Koutiri, I., Bourgeois, S. *Phys. Rev. B: Condens. Matter Mater. Phys.,* 2012, **86**, 224102.
52. Saha, D., Jensen, K. M. Ø., Tyrsted, C., Bøjesen, E. D., Mamakhel, A. H., Dippel, A.-C., Christensen, M., Iversen, B. B. *Angew. Chem., Int. Ed.,* 2014, **53**, 3667−3670.
53. Li, Y. H., Liu, P. F., Pan, L. F., Wang, H. F., Yang, Z. Z., Zheng, L. R., Hu, P., Zhao, H. J., Gu, L., Yang, H. G. *Nat. Commun.,* 2015, **6**, 8064.
54. Zhang, N., Li, X., Ye, H., Chen, S., Ju, H., Liu, D., Lin, Y., Ye, W., Wang, C., Xu, Q., Zhu, J., Song, L., Jiang, J., Xiong, Y. *J. Am. Chem. Soc.,* 2016, **138**, 8928−8935.
55. Ren, Y., Zou, Y., Liu, Y., Zhou, X., Ma, J., Zhao, D., Wei, G., Ai, Y., Xi, S., Deng, Y. *Nat. Mater.,* 2020, **19**, 203−211.
56. Zhang, G., Wang, C., Mizukami, W., Hosomi, T., Nagashima, K., Yoshida, H., Nakamura, K., Takahashi, T., Kanani, M., Yasui, T., Aoki, Y., Baba, Y., Yanagida, T. *Nanoscale,* 2020, **12**, 9058–9066.